

STUDY ON AERODYNAMICS OF THE WING WITH FLAP INSPIRED FROM BIRD COVERTS

Xiulai Xu[1,2,3], Wenqing Yang[1,2,3,*], Jianlin Xuan[1,2,3]

[1]School of Aeronautics, Northwestern Polytechnical University, Xi' an 710072, China
[2]Shenzhen Research Institute of Northwestern Polytechnical University, Shenzhen 518057, China
[3]National Key Laboratory of Aircraft Configuration Design, Xi' an 710072, China

Abstract

To address the long-standing challenge of flow separation and aerodynamic stall in bird-inspired flapping-wing air vehicles at high angles of attack, this study investigates the dynamic aerodynamic regulation mechanisms inspired by avian covert feathers. A biomimetic covert structure, simplified as a flat plate, is integrated onto the suction surface of a NACA0012 airfoil. Utilizing the overset grid method, two-dimensional unsteady numerical simulations and comprehensive multi-parameter analyses are systematically conducted. The results indicate that in the pre-stall regime (at a 10° angle of attack), the deployed covert induces a distinct physical blockage effect that prematurely redirects the oncoming flow, thereby deteriorating the lift coefficient. Conversely, in the post-stall regime (at a 20° angle of attack), the bio-inspired covert exhibits a pronounced, non-linear regulatory efficacy. Timely deployment of the covert effectively reconfigures local detached vortex structures and mitigates massive boundary layer separation. Consequently, a maximum enhancement of 25.93% in the lift coefficient is achieved under a specific parameter configuration (L/c=0.7, α=45°). This work clarifies the underlying aerodynamic mechanisms of covert-based flow control, offering crucial insights for the optimal design of next-generation ornithopters.

Keywords: Bio-inspired covert feathers; Stall control; Numerical simulation; Unsteady aerodynamics

1. Introduction

Through evolution and natural selection, organisms in nature have developed a myriad of structures and functions, whose exceptional capabilities have consistently served as a vital source of inspiration for human technological advancements. Among these fascinating biological talents, the flight capability of birds is particularly conspicuous due to its high efficiency, superb maneuverability, and robust adaptability, remaining a long-sought goal for humans to replicate and master.Avian flight does not adhere to a single pattern but exhibits remarkable diversity. Depending on their physiological structures, habitats, and flight environments, different species have evolved distinct flight modes, such as gliding, hovering, diving, and high-speed cruising [1,2].This behavioral diversity in flight is fundamentally rooted in wing architecture. Rather than being a rigid monolithic entity, a bird's wing is covered with a wide variety of functionally distinct feathers, which constitute a multi-level system capable of both passive and active adjustments.

In recent years, researchers have dedicated significant efforts to developing bird-inspired flapping-wing air vehicles (ornithopters). Their potential applications in fields such as near-ground reconnaissance and environmental monitoring in confined spaces have garnered considerable attention; however, these devices still face numerous challenges [3–5].For instance, under high-angle-of-attack flight conditions—such as low-speed takeoff/landing and close-range obstacle avoidance—conventional rigid or simple flexible wing surfaces are prone to severe flow separation. This phenomenon, wherein the boundary layer prematurely detaches from the wing surface, triggers a catastrophic drop in lift known as high-AoA stall, a deficiency that directly limits the vehicle's adaptability to complex environments. To truly replicate the high efficiency and agility of avian flight, merely mimicking macroscopic flapping motions is far from sufficient; instead, a deep

investigation into the microscopic cooperative regulation mechanisms of feathers is imperative.

Through long-term evolutionary adaptation, birds have precisely developed a coping strategy centered on the dynamic regulation of covert feathers. As illustrated in Fig. 1, when encountering high-angle-of-attack flight or flow disturbances, the timely deployment of covert feathers can disrupt the continuous separation of the boundary layer, thereby delaying stall and extending the critical angle of attack [6]. Concurrently, the hierarchical configuration of these coverts establishes a multi-scale flow control interface that mitigates the adverse effects of separated vortices, thereby maintaining a stable lift output even under high-angle-of-attack conditions.

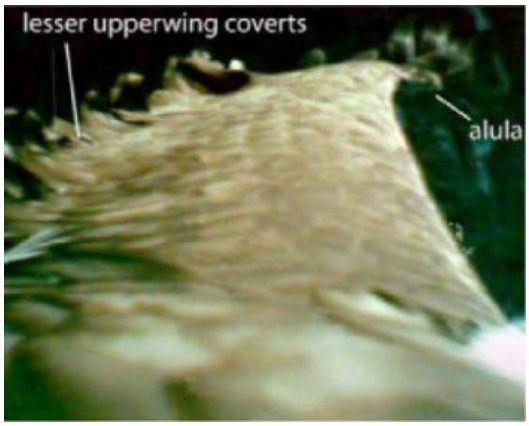


Figure 1 – The active elevation of the coverts on the upper wing surface.

Consequently, integrating covert-like movable structures onto artificial airfoil surfaces has emerged as a prominent research hotspot. These structures can regulate the external flow field through either active or passive means, thereby imparting superior aerodynamic performance to the vehicles under unsteady flow conditions compared to conventional flapping-wing configurations. Currently, drawing on the morphological architecture and distribution characteristics of natural avian coverts as a blueprint, researchers have conducted extensive experimental explorations and mechanistic elucidations, yielding a series of foundational insights [7–10].

However, a comprehensive survey of the state-of-the-art literature reveals several critical issues that remain unresolved; among these, research on active coverts is exceptionally scarce [11]. While existing studies have predominantly focused on the aerodynamic effects and kinematic characteristics of passive coverts [12–14], investigations into their active control mechanisms and dynamic regulation efficacy remain severely limited. Consequently, the core mechanisms and pivotal roles of active coverts in flight attitude regulation and aerodynamic performance optimization have yet to be fully elucidated.

To address the fundamental deficiencies in current bio-inspired covert research, this study focuses on the NACA0012 airfoil to systematically investigate the regulation laws of covert control parameters—specifically deployment position and angles—on the aerodynamic performance. By clarifying the coupled aerodynamic-kinematic mechanism between the covert and the main wing, this work establishes a baseline framework to support subsequent advancements in active bio-inspired covert deployment.

2. Geometric Configuration and Computational Setup

2.1 Geometric Model of the Bio-inspired Covert

To systematically investigate the complex aerodynamic effects and flow-control mechanisms induced by the bio-inspired covert on the airfoil performance, a detailed two-dimensional geometric and kinematic model was successfully established. The classic NACA0012 symmetric airfoil is employed as the primary main wing component, with the novel bio-inspired covert feather integrated onto its upper suction surface to interact with the boundary layer. For computational efficiency and simplicity, the covert is idealized as a rigid flat plate possessing a characteristic length fixed at $0.1c$ (where c explicitly denotes the baseline airfoil chord length). To precisely

quantify and trace the spatial positioning as well as the instantaneous attitude variations of the covert during operation, its kinematic motion is modeled as a single-degree-of-freedom rigid deflection around a fixed hinge point. The comprehensive geometric configuration, coordinate system, and structural layout of the entire bio-inspired airfoil assembly are schematically illustrated in detail in Fig. 2.

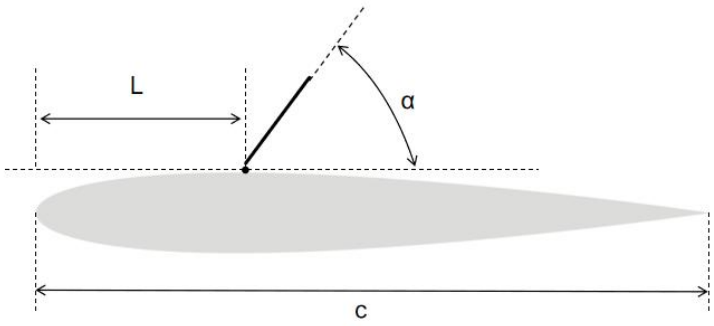


Figure 2 – Comprehensive geometric configuration of the airfoil with a bio-inspired covert

Where c denotes the airfoil chord length, L represents the distance from the leading edge to the bio-inspired feather, and α is the deployment angle of the feather. The primary geometric parameters of the bio-inspired feather device are summarized in Table 1.

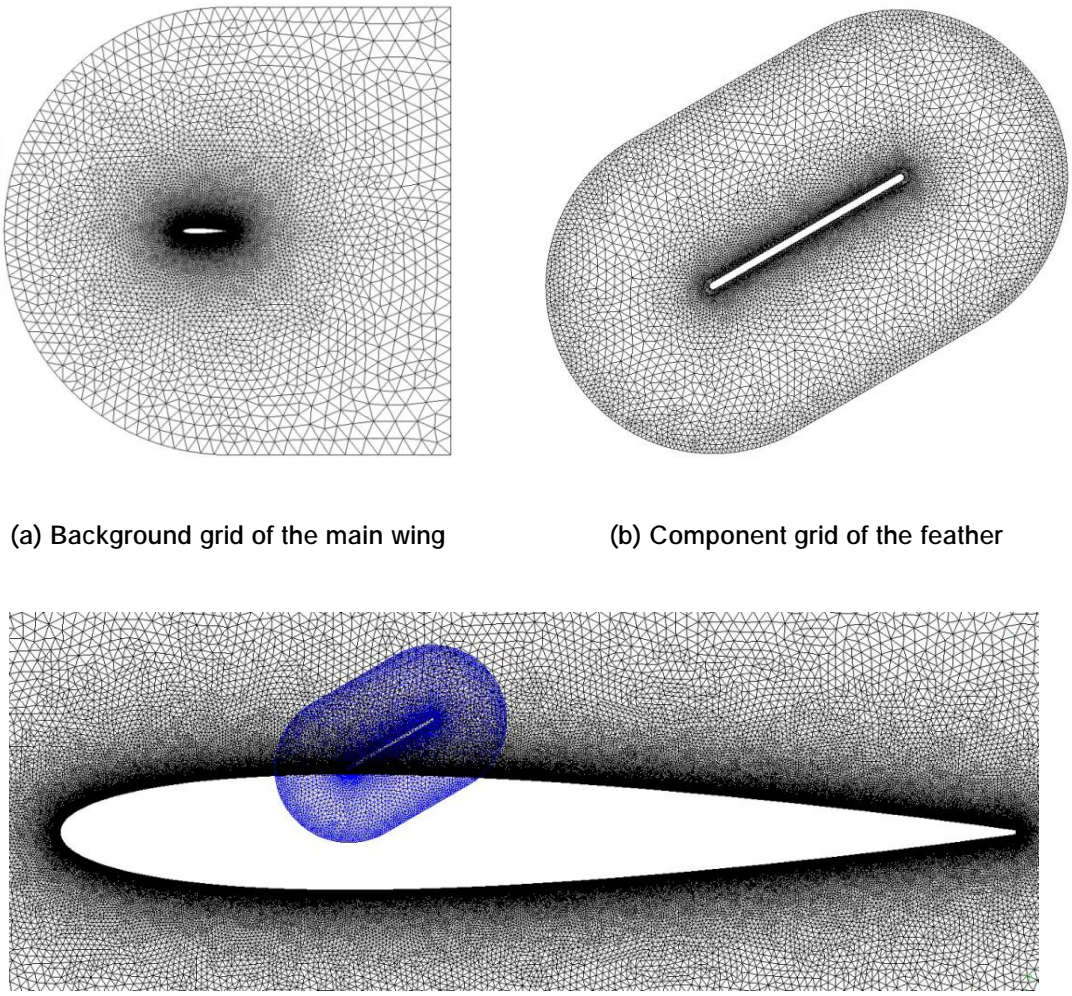
Table 1 – Geometric parameters of the airfoil model with bio-inspired feathers.

Parameter	Symbol	Value / Range
Airfoil chord length	c	0.15m
Distance of feather from leading edge	L	0.3c,0.5c,0.7c,0.9c
Initial deployment angle of feather	α	30°,45°,60°

This specific section is dedicated to systematically evaluating the profound effects of two core geometric design parameters—namely, the relative distance of the bio-inspired feather from the leading edge and its initial deployment angle—on the overall aerodynamic performance of the modified airfoil. Through comprehensive numerical simulations encompassing a wide range of multi-parameter combinations, this study aims to identify and isolate the optimal parameter configurations across various angles of attack. Consequently, this investigation serves to clarify the optimal aerodynamic matching mechanism and synergistic relationship between the fixed bio-inspired feather and the primary main wing.

2.2 Mesh Generation and Numerical Setup

For the two-dimensional (2D) simulations, the overset mesh method is employed to resolve the flow field around the bio-inspired feathered airfoil.As schematically illustrated in Figure 3, the comprehensive overset grid topology for the NACA 0012 airfoil is detailed, where Figures 3(a), 3(b), and 3(c) explicitly present the corresponding background grid of the main wing, the distinct component grid of the feather, and the fully assembled grid at the wing–feather interface zone, respectively. To ensure the accurate capture of the complex boundary layer flows near the solid wall boundaries, the first-layer grid spacing implemented on both the main wing and feather surfaces is rigidly constrained to satisfy $y+ \approx 1$.



(a) Background grid of the main wing

(b) Component grid of the feather

(c) Assembled grid at the wing–feather interface

Figure 3 – Overset mesh topology for the NACA 0012 airfoil system.

Regarding boundary conditions and computational cases, velocity inlet and pressure outlet conditions are applied to the far-field boundaries of the computational domain. The freestream velocity is set to 5 m/s. Numerical simulations are performed at two representative angles of attack (AOAs), θ = 10° and 20°, which correspond to the pre-stall and post-stall regimes of the baseline airfoil, respectively. These cases are selected to compare and analyze the flow control efficacy of the bio-inspired feather under distinct aerodynamic loads.

To resolve the governing equations, a fully second-order upwind spatial discretization scheme is employed for the momentum, turbulent kinetic energy, and specific dissipation rate terms. Pressure–velocity coupling is achieved via the Coupled algorithm, while a second-order scheme is applied for pressure interpolation. Temporal discretization is handled using a first-order implicit scheme. Furthermore, inner time sub-iterations are utilized to minimize linearization and factorization errors, thereby ensuring the convergence of the unsteady simulations.

2.3 Numerical Verification and Validation

2.3.1 Validation of the Numerical Solver

To ensure the reliability of the numerical method, validation of the computational solver was first performed. In the baseline simulations, the lift coefficient (C_L) of the clean NACA 0012 airfoil was evaluated as a function of the angle of attack (α) at a freestream velocity of 5 m/s. The computed results are compared with the numerical simulations of Lee and Tank [15,16] as well as the experimental data of Tomohisa and Jardin [17], as illustrated in Fig. 4. The comparison

indicates that the calculated C_L curve exhibits excellent agreement with both the experimental and numerical data from the literature. The minimal discrepancy confirms the accuracy and fidelity of the present solver in predicting the aerodynamic characteristics of the airfoil.

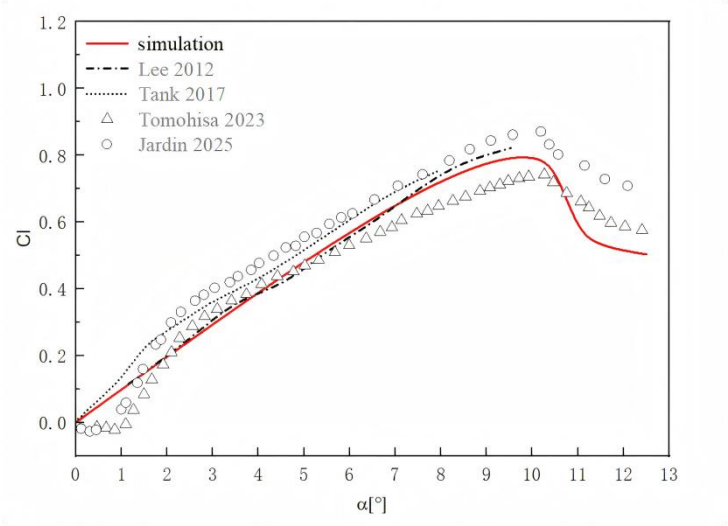


Figure 4 – Lift coefficient (C_L) versus angle of attack (α).

2.3.2 Grid and Time-Step Sensitivity Verification

In the subsequent verification of grid and time-step independence, unsteady moving cases are consistently employed for evaluation. The numerical tests are conducted at a Reynolds number of Re = 1.35×10^5. The airfoil executes a pure pitching motion around its quarter-chord pivot axis, with a freestream velocity of 15 m/s and a reduced frequency of k = 0.1. The time-dependent variation of the angle of attack (α) follows a sinusoidal function:

$$\alpha(t)=10°+15°\sin(2\pi ft) \quad (1)$$

The initial angle of attack (AOA) of the flapping airfoil is set to 10° with a pitching amplitude of 15°, yielding an AOA variation range from -5° to 25°. Three grid systems with different resolutions are utilized to evaluate grid dependency, the detailed statistics of which are summarized in Table 2.

Table 2 – Comparison of mesh statistics for the three grid systems

Grid Resolution	Background Grid	Overset Grid	Total Elements
Coarse	7146	139553	146699
Medium	10636	218167	225313
Fine	20788	271313	292101

For the grid independence study, the time step size is fixed at 1,000 steps per flapping cycle. Figure 5 displays the comparison of lift and drag coefficients (C_L and C_D) across the three grid systems. It is observed that under the identical time step, the aerodynamic coefficients predicted by the coarse grid exhibit a prominent discrepancy compared to the other two configurations. Conversely, the results obtained from the medium and fine grids achieve excellent agreement, with no discernible differences in either lift or drag histories. Balancing computational accuracy against resources, the medium grid system containing approximately 225,000 cells is selected for all subsequent investigations.

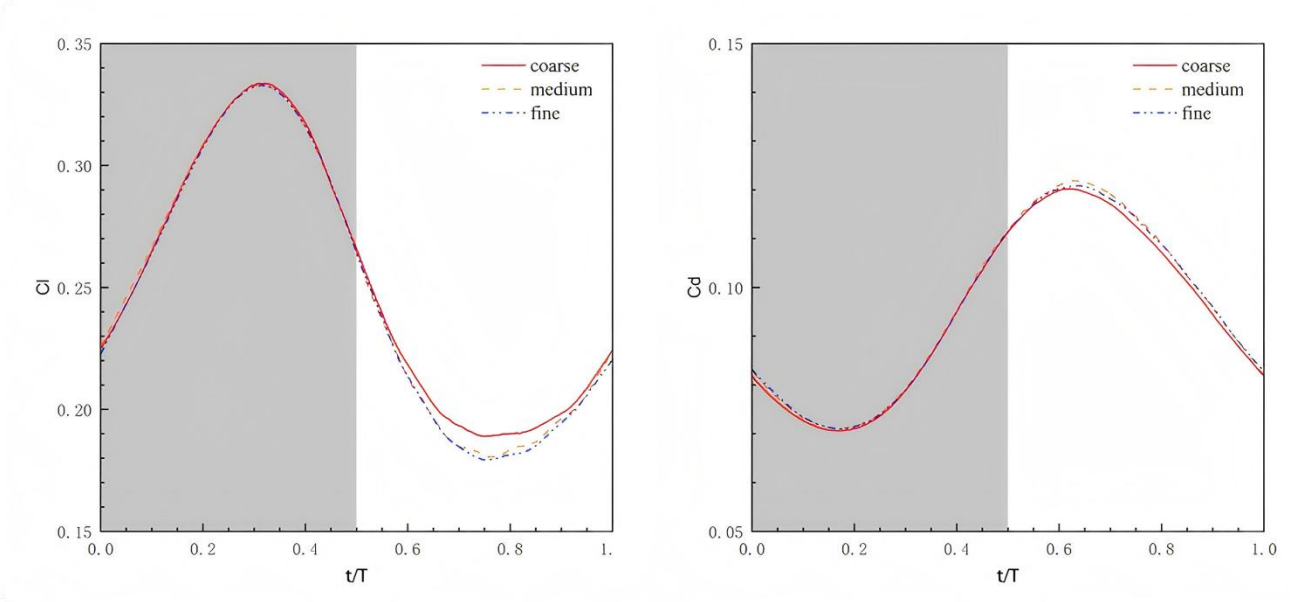


Figure 5 – Grid independence study.

Having established the grid density, a subsequent time-step independence study is conducted using the medium mesh to determine an optimal temporal resolution that balances computational efficiency and numerical accuracy. Three distinct time-step sizes, corresponding to 500, 1,000, and 2,000 steps per flapping cycle, are evaluated and compared.

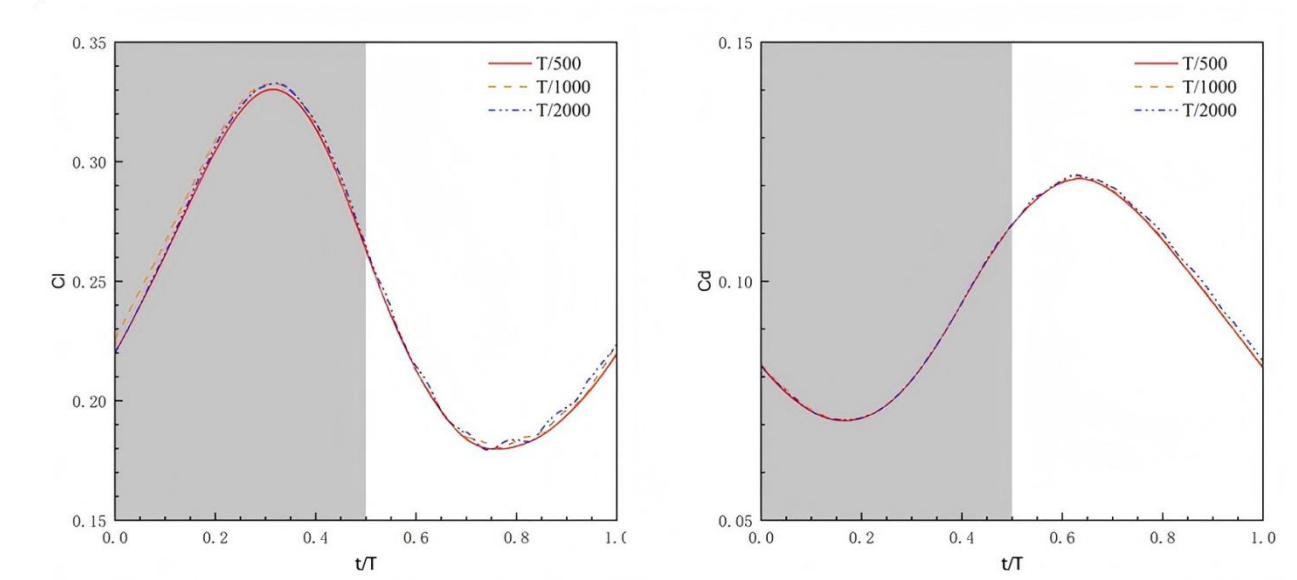


Figure 6 – Time-step independence study

Figure 6 presents the comparison of lift and drag coefficients calculated under the three distinct time step sizes. It can be observed that the temporal resolution of 500 steps per cycle fails to precisely capture the peak values of the lift coefficient, exhibiting a slight deviation from the other two cases. Conversely, the aerodynamic curves obtained from the temporal resolutions of 1,000 and 2,000 steps per cycle virtually overlap, yielding a negligible discrepancy. Consequently, a time step size of 1,000 steps per cycle is selected for all subsequent investigations to ensure both numerical accuracy and computational efficiency.

3. Results

Regarding the solver validation results, the NACA 0012 airfoil exhibits a stall angle of attack (AOA) between 10° and 11° at a free-stream velocity of 5 m/s. Consequently, AOAs of 10° and 20° are designated as the characteristic representatives of pre-stall and post-stall flow regimes, respectively, to comprehensively investigate the underlying aerodynamic mechanisms.

3.1 Aerodynamic Analysis of Airfoil with Covert Feathers at 10° Angle of Attack

3.1.1 Analysis of Aerodynamic Coefficients

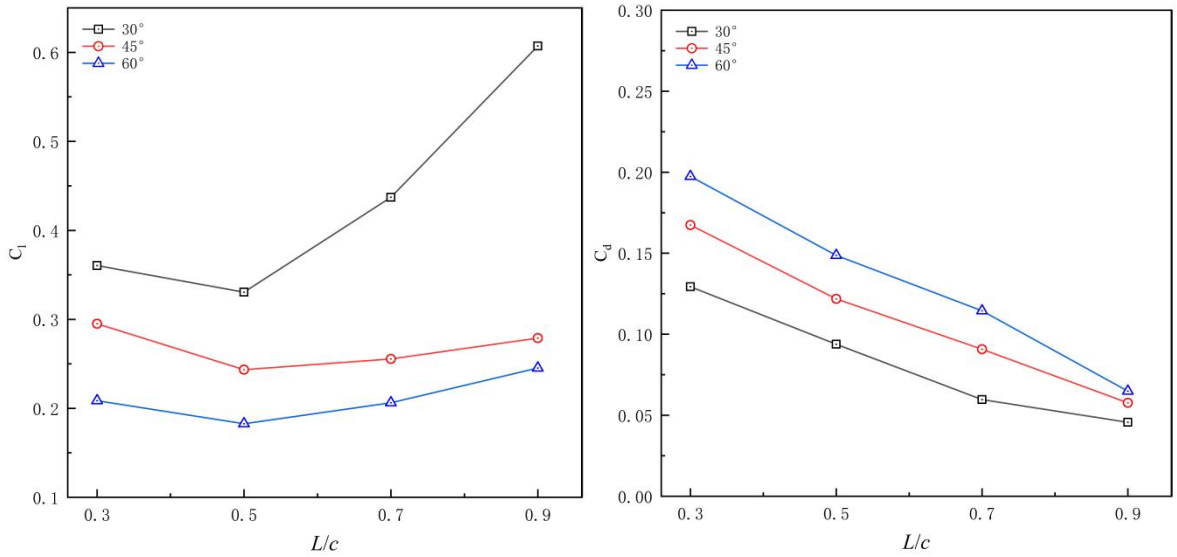
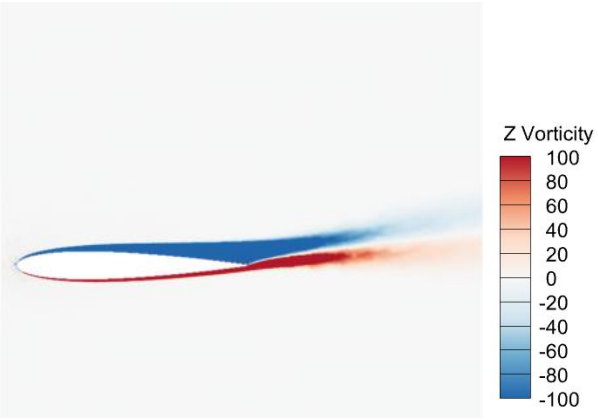


Figure 7 – Lift and drag coefficient curves for the covert-feathered airfoil at an angle of attack of 10°.

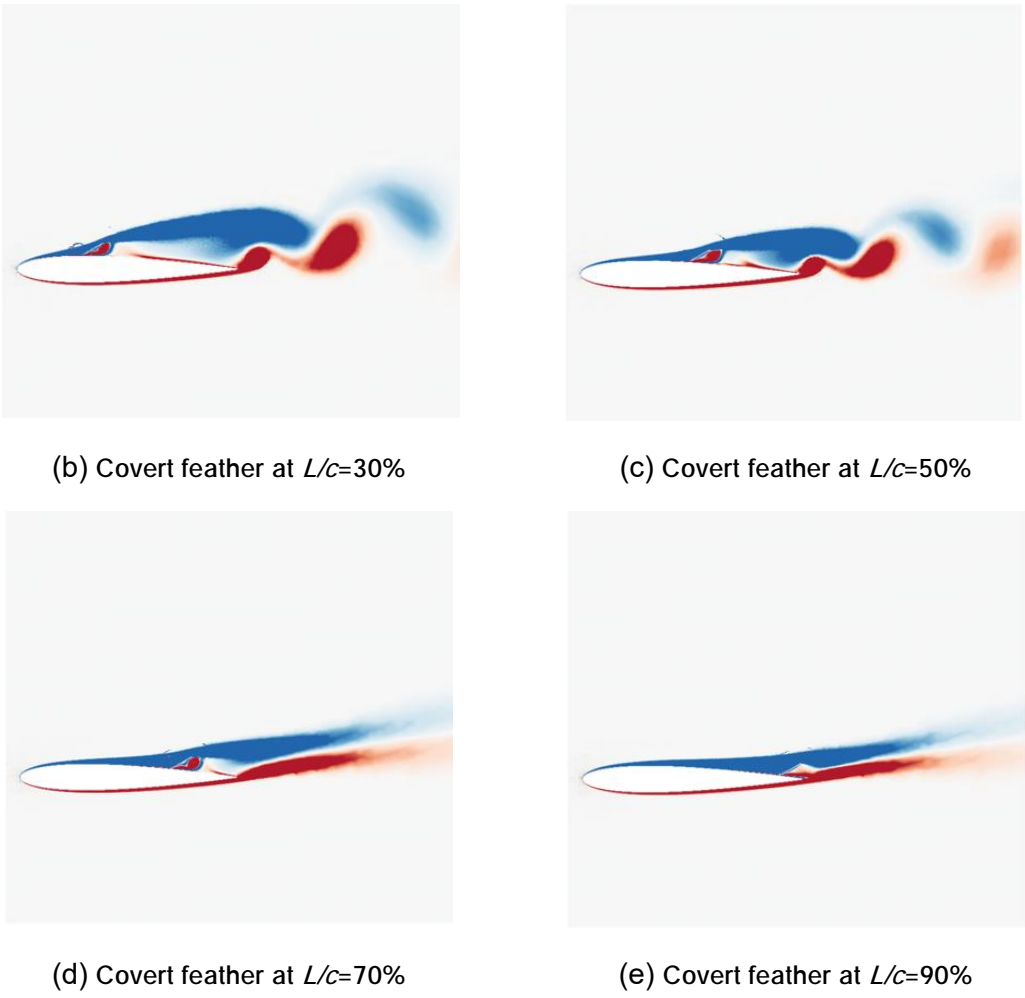
Figure 7 illustrates the effects of various installation positions and deployment angles on the lift coefficient (C_L) of the feathered airfoil under the pre-stall condition ($\theta = 10°$). The aerodynamic coefficient curves reveal that introducing covert feathers prior to stall generally exerts an adverse impact on the aerodynamic performance, characterized by a comprehensive reduction in C_L. Further analysis indicates that the degree of aerodynamic degradation is closely coupled with the installation location and deployment angle of the feathers: the mitigation of C_L gradually diminishes as the installation position shifts downstream (increasing L/c) or as the deployment angle decreases. This suggests that under pre-stall conditions, the covert feathers should ideally maintain a closed position with a minimal angle or be deployed near the trailing edge to minimize aerodynamic penalties.

3.1.2 Underlying Mechanisms of the Effects of Covert Feather Installation Locations

To elucidate the underlying mechanisms responsible for the aforementioned variations in aerodynamic loads, this section further provides a comparative analysis from the perspective of flow-field vorticity distribution evolution.



(a) Baseline airfoil without covert feathers



(b) Covert feather at *L/c*=30% (c) Covert feather at *L/c*=50%

(d) Covert feather at *L/c*=70% (e) Covert feather at *L/c*=90%

Figure 8 – Vorticity contours at various covert feather locations.

Figure 8 presents the Z-vorticity contours for both the baseline airfoil and the airfoil incorporated with covert feathers at a fixed deployment angle of 30°, positioned at various chordwise locations (30°, 50°, 70°, and 90°).

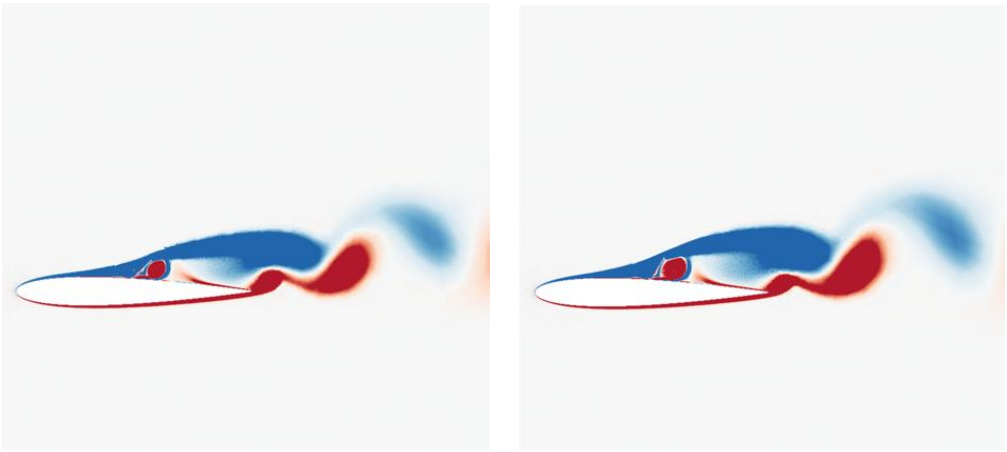
At an angle of attack of 10°, the baseline airfoil without covert feathers exhibits an ideal attached flow state. Specifically, both the negative vorticity shear layer on the upper surface and the positive vorticity shear layer on the lower surface adhere closely to the airfoil contour, with no large-scale flow separation observed. The wake shear layer merging at the trailing edge remains narrow and stable, yielding a minimized pressure drag and a sufficient flow-field circulation, which consequently maintains a high baseline lift.

However, the introduction of the covert feathers fixed at a 30° deployment angle on the upper surface disrupts the originally smooth, viscous attached flow. When positioned at the fore-and-mid chord locations (L/c = 0.3 and 0.5, as shown in Figs. 8b and 8c), the high-velocity oncoming flow on the suction surface impinges on the feather structure, forcing an early onset of large-scale, irreversible forced flow separation in the boundary layer. This separation further induces a prominent alternately shedding von Kármán vortex street downstream of the feather. Such extensive separated shear layers occupy the mid-to-aft upper surface, suppressing the formation of an effective low-pressure region on the suction surface. Consequently, the flow-field circulation is severely compromised, accompanied by a sharp increase in pressure drag, thereby leading to a drastic attenuation of the lift coefficient.

In contrast, when the covert feathers are deployed at the mid-to-aft chord locations (L/c = 0.7 and 0.9, as shown in Figs. 8d and 8e), the negative vorticity bands over the leading-edge and mid-chord regions reattach to the suction surface as the deployment location shifts downstream. This reattachment effectively preserves the high suction (low-pressure) region near the leading edge. The flow separation and vortex shedding induced by the feathers are confined to a narrow region near the trailing edge. Consequently, although the aerodynamic loads remain lower than those of the baseline airfoil, the magnitude of this reduction is significantly mitigated.

3.1.3 Underlying Mechanisms of the Effects of Covert Feather Deployment Angles

To further explore the disturbance mechanisms of the deployment angle on the pre-stall flow field, Figure 8 provides a comparison of Z-vorticity contours when the covert feathers, positioned at the70% chordwise location, are deployed at increased angles of 45° and 60°.



(a) Covert feather at α=45° (b) Covert feather at α=60°

Figure 9 – Vorticity contours at various covert feather deployment angles.

As the covert feather deployment angle increases beyond 30°, the blockage effect on the upper suction surface is significantly amplified. This expansion in the frontal aerodynamic blockage area severely obstructs the oncoming flow, thereby inducing more pronounced flow separation within the flow field.

Taking the 70% chordwise location case as an example, the spatial extent of the separated flow is markedly suppressed at a moderate deployment angle of 30°, allowing the flow field over the fore-and-mid chord regions to remain well attached. Conversely, when the deployment angle abruptly increases to 45°, the intense physical blockage triggers a substantial upstream propagation of the adverse pressure gradient. Consequently, well before reaching the feather location at 70% chord, the oncoming flow undergoes a premature global liftoff and detaches from the airfoil surface around the mid-chord region (approximately 50% chord).Downstream of the covert feather and within the wake region, a circular positive-vorticity recirculation structure and large-scale, alternately shedding Kármán vortex streets are generated. A similar flow-field reconfiguration behavior is observed when the deployment angle is further increased to 60°.These microscopic flow-field evolutions provide a sound physical mechanism that accounts for the lift coefficient curve characteristics shown in Figure 7, wherein larger deployment angles yield more severe aerodynamic penalties.

In summary, at a 10° angle of attack (the pre-stall regime), the boundary layer on the suction surface of the baseline airfoil remains well-developed, and the attached flow maintains a smooth and continuous topology. The introduction of the flat-plate bio-inspired covert under these conditions essentially introduces an artificial 'micro-step' on the otherwise streamlined boundary. From a fluid dynamics perspective, the leading edge of the deployed covert exerts a significant stagnation effect on the oncoming high-kinetic-energy attached flow. This causes the local kinetic energy to convert into pressure energy, leading to a localized spike in static pressure. This abrupt geometric disturbance not only disrupts the continuity of the streamlines—forcing the upstream flow to redirect prematurely outward—but also induces an adverse pressure gradient upstream of the covert structure. Consequently, the low-momentum fluid within the boundary layer fails to overcome this downstream pressure resistance, thereby triggering unnecessary local weak separation. More importantly, the outward deflection of the streamlines and the subsequent pressure rise near the leading edge substantially diminish the 'suction effect' within the airfoil's primary low-pressure suction peak, effectively deteriorating the pressure differential between the upper and lower surfaces. This physical blockage-induced alteration of the flow topology and the overall elevation of suction-surface pressure constitute the fundamental intrinsic mechanism responsible for the

comprehensive degradation of the lift coefficient across all parametric configurations at a 10° angle of attack.

3.2 Aerodynamic Analysis of Airfoil with Covert Feathers at 20° Angle of Attack

3.2.1 Analysis of Aerodynamic Coefficients

Under the post-stall regime at a large angle of attack (θ = 20°), the effects of varying installation locations and deployment angles on the lift coefficient (C_L) of the covert-feathered airfoil are illustrated in Figure 10. As observed from the lift coefficient curves, the introduction of the bionic covert feathers exerts a significant nonlinear modulation on the aerodynamic performance under stall conditions. Overall, as the installation location shifts downstream, the lift coefficient exhibits a distinct evolutionary trend characterized by an initial plateau, followed by a dramatic surge, and ultimately a sharp decline. This indicates that the installation location plays a dominant role in altering the lift characteristics, whereas the deployment angle possesses a relatively minor influence.

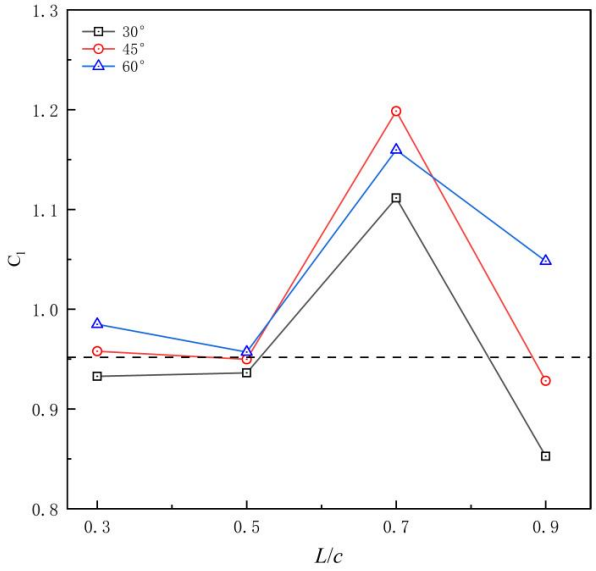


Figure 10 – Lift coefficient curves for the covert-feathered airfoil at an angle of attack of 20°.

When the feathers are arranged at the 70%c chordwise location, the lift coefficients across all investigated deployment angles consistently reach their global peaks, which are prominently higher than the baseline value of the clean airfoil, identifying this location as the optimal lift-enhancement control zone. In the fore-and-mid chord regions, the aerodynamic lift for cases with larger deployment angles (45° and 60°) remains above the baseline. Conversely, in the vicinity of the trailing edge, the lift coefficients for smaller deployment angles drop below the baseline value, with the sole exception of the 60° large-angle case, which still maintains a noticeable lift-enhancement effect.

Consequently, the optimal aerodynamic configuration for this airfoil at an angle of attack of 20° is determined to be the installation location of 70%c coupled with a deployment angle of 45°.

3.2.2 Underlying Mechanisms of the Effects of Covert Feather Installation Locations

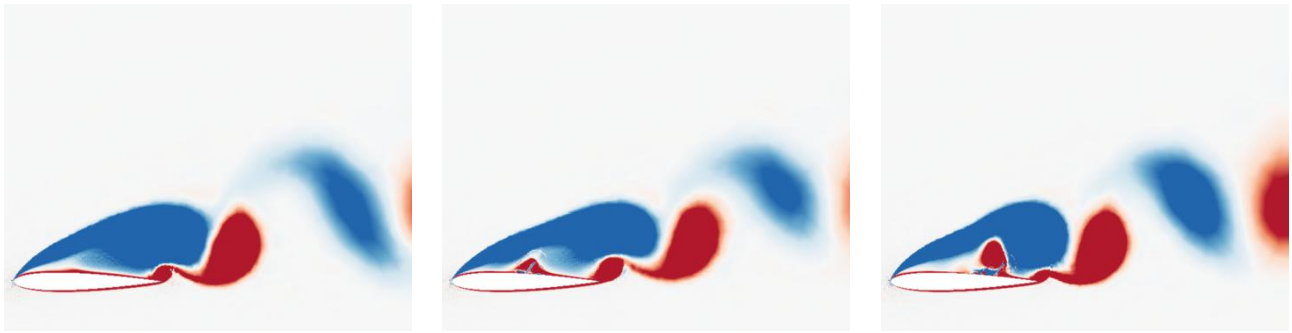
Figure 11 presents the Z-vorticity contours for both the baseline and covert-feathered airfoils under various configurations at θ = 20°.

Serving as the control group, Figure 11a illustrates the flow field of the clean baseline airfoil. At a large angle of attack of 20°, the baseline airfoil surface enters a fully stalled state. The boundary-layer flow undergoes massive, large-scale separation initiated near the leading edge, forming a separated shear layer and a comprehensive separation zone that pitch substantially upward and envelop nearly the entire upper suction surface. Upon merging at the trailing edge with the attached, high-pressure flow from the pressure surface, this separated flow evolves into periodically and alternately shedding von Kármán vortex streets. Such severe separation and vortex shedding drastically diminish the magnitude of suction on the upper surface, leading to a substantial loss of lift accompanied by pronounced aerodynamic load fluctuations.

When the covert feather is positioned at the 50%c chordwise location, as depicted in Figure 11b, it is clearly observed that the feather structure is entirely embedded within the pre-existing

leading-edge separation bubble. Buried deep inside this dead-flow zone, the feather is completely isolated from the external high-momentum freestream. Consequently, it can neither suppress the upstream leading-edge separation nor modulate the shedding intensity and frequency of the trailing-edge vortices. Failing to disrupt or reconfigure the original flow topology, the presence of the feather introduces negligible alterations to the surface pressure distribution, thereby yielding an insubstantial change in the lift coefficient.

Conversely, shifting the covert feather further downstream to the 70%c location triggers a fundamental reconfiguration of the flow field, which constitutes the primary mechanism underlying the enhancement of the lift coefficient. The 70%c location coincides precisely with the transitional region where the massive separation zone evolves into the wake. Upon deploying the feather at a 45° angle at this critical junction, its windward surface interacts strongly with the separated flow. This interaction effectively obstructs the spanwise and downward diffusion of the shear layer, while concurrently inducing a localized positive-vorticity region upstream of the feather. This induced structure successfully intercepts the chaotic, large-scale separated flow originating from the leading edge, forcing the flow to reattach onto the airfoil surface as it passes over the feather. Consequently, local flow-field reconstruction and suction intensification are achieved on the upper surface downstream of the feather. This localized, bionic-structure-induced vortex modulation effectively stabilizes the flow state over the mid-to-aft sections of the upper surface, thereby optimizing the low-pressure distribution in the trailing region.



(a) Baseline airfoil without covert feathers

(b) Covert feather at L/c=50%

(c) Covert feather at L/c=70%

Figure 11 – Vorticity contours at various covert feather locations.

In summary, at a 20° high angle of attack (the post-stall regime), the baseline airfoil undergoes severe and unstable dynamic stall vortex shedding induced by the violent separation of the leading-edge shear layer. Under these challenging conditions, the core aerodynamic control mechanism of the bio-inspired covert structure lies in its capacity for localized 'flow reconfiguration and vortex control.' The spatial geometric shielding of the deployed covert essentially establishes a physical barrier on the mid-to-aft section of the suction surface. This barrier not only effectively intercepts the large-scale detached vortices rolling downstream from the leading edge and restricts the upstream reversal of the separated backflow, but it also 'anchors' and breaks down the highly periodic, unsteady large vortex structures into smaller-scale, attached high-frequency micro-structures. This reconfiguration of the flow topology partially rejuvenates the flow over the rear portion of the airfoil, re-establishing a localized low-pressure suction region and macroscopically manifesting as stall delay and a significant non-linear enhancement of the lift coefficient.

4. Conclusions

Inspired by the dynamic aerodynamic modulation mechanisms of avian wing covert feathers, this study focuses on the critical bottleneck of flow separation and stall vulnerability in airfoils at large angles of attack. Two-dimensional unsteady numerical simulations are conducted on a NACA 0012 airfoil incorporated with covert feathers utilizing the overset grid method. Under a freestream velocity of 5 m/s, the aerodynamic modulation characteristics are systematically investigated across various feather installation locations (L= 0.3c, 0.5c, 0.7c, and 0.9c) and initial deployment angles (θ= 30°, 45°, and 60°) under two typical flow regimes: pre-stall (θ= 10°) and post-stall (θ= 20°). Through detailed analyses of the lift and drag coefficients, alongside the evolution of the flow-field microscopic vorticity, the following core conclusions are drawn:

(1) Pre-stall regime (θ= 10 °): The introduction of fixed-angle covert feathers induces a detrimental physical blockage effect. The feathers expand the frontal aerodynamic blockage area and trigger a premature upstream propagation of the adverse pressure gradient, forcing the flow to detach early from the airfoil surface, which manifests as a comprehensive degradation of the lift coefficient. This aerodynamic penalty is progressively mitigated as the installation location shifts downstream (increased L/c) or as the deployment angle decreases.

(2) Post-stall regime (θ= 20 °): The introduction of the bionic covert feathers exerts a pronounced nonlinear modulation on the airfoil aerodynamic performance. The deployment of the feathers disrupts the massive boundary-layer separation and reconstructs the localized vortex topology. Under specific geometric configurations, this modulation successfully delays stall propagation, thereby maintaining or optimizing a stable lift output.

Although realistic covert feathers undergo dynamic flapping rather than remaining entirely rigid, the optimization of feather kinematic parameters remains beyond the scope of this paper and will be addressed in future studies. This investigation successfully identifies the effective incoming flow conditions and determines the optimal static parameter configuration for bionic covert feathers. These findings lay a solid foundation for incorporating active flow control strategies and exploring the flapping aerodynamics of covert feathers in subsequent research.

5. Contact Author Email Address

Mailto: yangwenqing@nwpu.edu.cn

6. Copyright Statement

The authors confirm that they, and/or their company or organization, hold copyright on all of the original material included in this paper. The authors also confirm that they have obtained permission, from the copyright holder of any third party material included in this paper, to publish it as part of their paper. The authors confirm that they give permission, or have obtained permission from the copyright holder of this paper, for the publication and distribution of this paper as part of the ICAS proceedings or as individual off-prints from the proceedings.

7. Acknowledgments

This study was supported by the National Natural Science Foundation of China (No. 52275293).

References

[1] Lock, R. J., Burgess, S. C. & Vaidyanathan, R. Multi-modal locomotion: From animal to application. *Bioinspir. Biomim*, 9, 011001, 2013.

[2] Kadar F, Tatar M. *A Review on Mobile Robots with Multimodal Locomotion* [M].337-349,2023.

[3] Bie D, Li D, Xiang J, et al. Design, aerodynamic analysis and test flight of a bat-inspired tailless flapping wing unmanned aerial vehicle[J]. *Aerospace Science and Technology*, 112: 106557, 2021.

[4] Bin Abas, M. F., Bin Mohd Rafie, A. S., Bin Yusoff, H. & Bin Ahmad, K. A. Flapping wing micro-aerial-vehicle: Kinematics, membranes, and flapping mechanisms of ornithopter and insect flight. *Chinese Journal of Aeronautics* 29, 1159–1177, 2016.

[5] Rafee Nekoo, S. et al. A review on flapping-wing robots: Recent progress and challenges. *The International Journal of Robotics Research* 44, 2305–2339, 2025.

[6] Liebe, W. Der Auftrieb am Tragfliigel: Entstehung und Zusammenbruch[J]. *Aerokurier*, 12, 1520-1523, 1979.

[7] Carruthers A C, Thomas A, Taylor G K. Automatic aeroelastic devices in the wings of a steppe eagle Aquila nipalensis[J]. *Journal of Experimental Biology*, 210(Pt 23): 4136-4149, 2008.

[8] Duan C, Wissa A. Covert-inspired flaps for lift enhancement and stall mitigation. *Bioinspir Biomim*, 16(4): 046020, 2021.

[9] Johnston J, Gopalarathnam A. Investigation of a bio-inspired lift-enhancing effector on a 2D airfoil. *Bioinspir Biomim*, 7(3): 036003, 2012.

[10] Zekry, D. A., Nam, T., Gupta, R., Zhu, Y. & Wissa, A. A. Covert-inspired flaps: an experimental study to understand the interactions between upperwing and underwing covert feathers. *Bioinspir. Biomim,* 18, 046021, 2023.

[11] Rosti, M. E., Kamps, L., Bruecker, C., Omidyeganeh, M. & Pinelli, A. The PELskin project-part V: Towards the control of the flow around aerofoils at high angle of attack using a self-activated deployable flap. *Meccanica* 52, 1811–1824, 2017.

[12] Meyer, R. et al. Separation Control by Self-Activated Movable Flaps. *AIAA Journal* 45, 191–199, 2007.

[13] Yang, Y. et al. Interaction between vortex shedding and flap oscillation in separation control of a stalled aerofoil. *Aerospace Science and Technology* 163, 110300, 2025.

[14] Rosti, M. E., Omidyeganeh, M. & Pinelli, A. Passive control of the flow around unsteady aerofoils using a self-

activated deployable flap. *Journal of Turbulence* 19, 204–228, 2018.
[15] Lee, T.Su, Y. Y.Low Reynolds number airfoil aerodynamic loads determination via line integral of velocity obtained with particle image velocimetry[J].*Experiments in Fluids*, 53, (5): 1177-1190, 2012.
[16] Tank, J.Smith, L.Spedding, G. R.On the possibility (or lack thereof) of agreement between experiment and computation of flows over wings at moderate Reynolds number[J].*Interface Focus*, 7, (1): 20160076-20160076, 2017.
[17] Jardin, T., Ferrand, V. & Gowree, E. R. NACA0012 airfoil at Reynolds numbers between 50,000 and 140,000 — Part 1: Steady freestream. *International Journal of Heat and Fluid Flow* 112, 109655, 2025.